The wavelet transform as a tool for geophysical data integration

Kees Wapenaar[*], Ranajit Ghose, Gerrit Toxopeus and Jacob Fokkema
Department of Geotechnology, Delft University of Technology, P.O. Box 5028, 2600 GA Delft, The Netherlands
E-mail: {C.P.A.Wapenaar, R.Ghose, G.Toxopeus}@CiTG.TUDelft.NL

Abstract. In geophysical exploration different types of measurements are used to probe the same subsurface region. In this paper we show that the wavelet transform can aid the process of linking different data types.

The continuous wavelet transform, and in particular the analysis of amplitudes along wavelet transform modulus maxima lines, is a powerful tool to analyze the characteristic properties of local variations in a signal. The amplitude-versus-scale curve of a particular transition in a signal can be seen as its fingerprint. Hence, local variations in different data types can be linked by comparing their fingerprints in the wavelet transform domain. Insight in the physics underlying the different types of measurements is required to 'tune' the different wavelet transforms in such a way that a particular geological transition in the Earth's subsurface leaves the same fingerprint in the wavelet transform of each data type.

We discuss the wavelet transform as a tool for geophysical data integration for three situations. First we discuss how one can link the scale-dependent properties of outliers in borehole data to those of reflection events in surface seismic data. We use wave theory to derive relations between the two data types in the wavelet transform domain. Next we analyze the relation between the wavelet transforms of detailed geological models and (simulated) migrated seismic data, with the aim of improving the geological interpretation. A spatial resolution function provides the link between the wavelet transforms of the geological model and the migrated seismic data. Finally we consider the integration of geotechnical (cone penetration test) data with shallow shear wave seismic data. We illustrate with a real data example that specific geological features of the shallow subsurface can be identified in the wavelet transforms of both data types. We conclude that the wavelet transform can be used as a tool that aids the integration of different types of data.

1. Introduction

Over the last ten to fifteen years geophysical exploration has turned into an integrated discipline in which different types of data are combined to infer detailed information about the structure and properties of the Earth's subsurface. The integration is hampered by the fact that the different data types are obtained by different measurement techniques which are sensitive to different properties of the Earth's subsurface. Moreover, the different types of measurements are usually carried out at different scales. A well-known example is the problem of linking borehole data with surface seismic data. A tool lowered in a borehole measures amongst others the sound propagation velocity of the formation at ultrasonic frequencies with a depth interval of typically 15 cm. On the other hand, a seismic experiment carried out at the Earth's surface probes the geology of the subsurface with frequencies in the range of 10 to 100 Hertz, leading to a depth resolution of typically 50 m. Matching geological boundaries, appearing as reflection events in seismic data, to changes in the ultrasonic velocity measured in a borehole is a nontrivial task.

It is the aim of this paper to show that the wavelet transform can aid the process of linking different data types. The wavelet transform has proven to be a powerful tool to analyze the properties of local variations in a signal (Mallat and Hwang [13]). Herrmann [8,9] proposed to use this feature to characterize the properties of acoustic borehole data. In particular he showed that many outliers in these data exhibit a characteristic kind

*Corresponding author.

of scaling behavior. To be more specific, the strength of these outliers appears to vary in an approximately constant rate when they are observed as a function of scale (in a log-log representation). This rate of change may be seen as the fingerprint of the outlier. It is reasonable to assume that outliers in borehole data often correspond to geological transitions that act as reflectors for seismic waves. Hence, the process of matching outliers in borehole data to reflection events in surface seismic data will be aided by comparing their fingerprints [1] (i.e, their scaling properties). Of course, due to the different measurement techniques and the different scales of observation, this requires insight in the relation between the different types of data and their scaling properties.

Robinson [16] was among the geophysical pioneers who recognized that "a large part of basic seismic research is directed toward a better understanding of the physical processes involved in the seismic method". He was one of the first who showed that the geological information embedded in the recorded seismic signal can only be recovered if the processing algorithms are based on the physical models that describe the wave propagation in the earth. Consistent with this view he contributed to the field of seismic processing with applications on predictive decomposition, minimum delay, deconvolution and inversion to name a few. Especially in his last book [17] he gives a beautiful account of his contributions to seismic processing. It is in this spirit that we will not simply compare wavelet transforms of different data types but use the physics underlying the measurement techniques to tailor the wavelet transform for each data type. This allows an optimum comparison of the imprints of specific geological events in the wavelet transforms of the different types of measurements.

The setup of this paper is as follows. In Section 2 we briefly review the wavelet transform as a tool for analyzing the scaling properties of local variations in a signal (multi-scale analysis). This summarizes the method proposed by Mallat and Hwang [13] and part of the PhD work of Herrmann [8,9], who proposed to use this type of analysis for the characterization of borehole data. In Section 3 we use the acoustic wave equation to derive the relation between the scaling properties of borehole- and surface seismic data. We show with theory as well as with realistic numerical examples that the scaling parameters of outliers in borehole data can be matched with those of the seismic reflection

response. This section summarizes a paper by one of the authors [22] and also builds on the PhD work of Herrmann [8], Dessing [1], van Wijngaarden [20], Verhelst [21], and Goudswaard [6]. In Sections 4 and 5 we discuss new work. Recently Toxopeus et al. [19] proposed an improved interpretation of geological models with simulated migrated seismic data. In Section 4 we show that this interpretation is further aided by comparing the scale parameters of the geological models with those of the simulated migrated seismic data. In Section 5 we discuss the scaling analysis of geotechnical data [cone penetration test (CPT) data] and shallow seismic shear wave reflection data and show the correspondence of the scaling parameters of both data types at the hand of a real data example. This summarizes very recent work by Ghose and Goudswaard [4]. In Section 6 we present our conclusions.

2. Analysis of scaling properties with the wavelet transform

In this section we review the wavelet transform as a tool for analyzing the scaling properties of local variations in a signal (for more extensive discussions on the mathematical aspects of the wavelet transform we refer to Kaiser [10] and Mallat [12]). We define the continuous wavelet transform of a signal $c(z)$ as

$$\check{c}(\sigma, z) = \frac{1}{|\sigma|^\mu} \int_{-\infty}^{\infty} c(z') \, \psi\left(\frac{z' - z}{\sigma}\right) \mathrm{d}z', \quad (1)$$

where $\psi(z)$ is the analyzing wavelet which we choose to be real-valued, and σ is the scale parameter. The exponent μ in the normalization term $1/|\sigma|^\mu$ is often chosen equal to $1/2$ in order to make the transformation an isometry [11]. However, for the moment we do not specify μ and we choose convenient values for it later. We use the wavelet transform to analyze the following signal

$$c(z) = \begin{cases} c_1 |z/z_1|^\alpha \text{ for } z < 0 \\ c_2 |z/z_1|^\alpha \text{ for } z > 0, \end{cases} \quad (2)$$

which is shown in Fig. 1(a) for $\alpha = -0.4$, $c_1 = 800$, $c_2 = 1200$ and $z_1 = 5$. Note that this signal obeys the scaling relation

$$c(\sigma z) = \sigma^\alpha c(z), \quad (3)$$

for $\sigma > 0$, hence, $c(z)$ is *self-similar*. The exponent α is characteristic for the behavior of the signal $c(z)$ around its singular point $z = 0$. The wavelet transform $\check{c}(\sigma, z)$ is defined by Eq. (1) and is shown in Fig. 1(b).

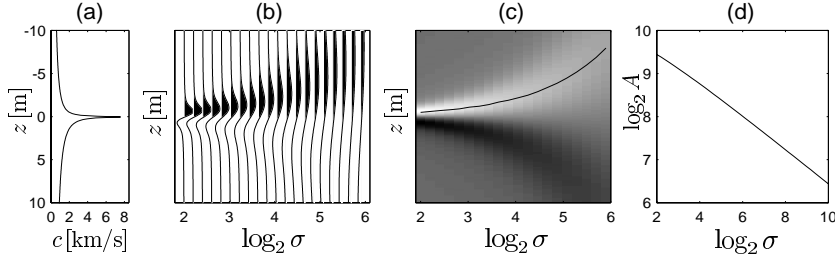[1] See Fig. 11 for a justification of the term 'fingerprint'.

Fig. 1. (a) Self-similar signal, described by Eq. (2), with $\alpha = -0.4$. (b) Continuous wavelet transform of the signal in figure a. (c) Wavelet transform modulus maxima line WTMML, obtained from figure b. (d) Amplitude-versus-scale (AVS) curve, measured along the modulus maxima line in figure c. The slope ($\alpha = -0.4$) corresponds to the singularity exponent of the signal in figure a.
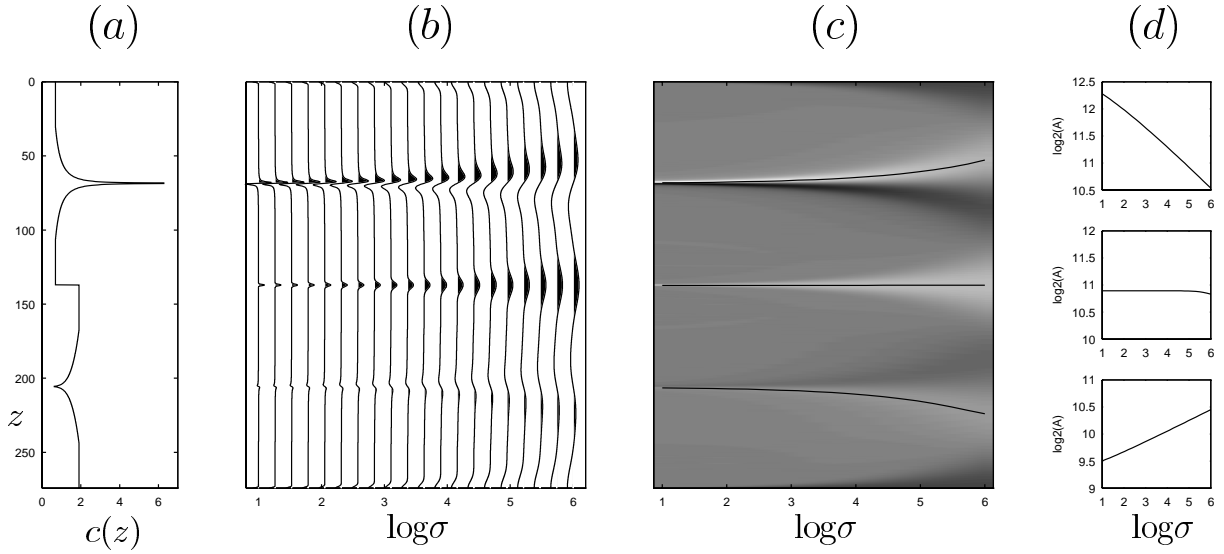

Fig. 2. (a) Three shifted versions of the self-similar signal, described by Eq. (2), with $\alpha = -0.4$, 0 and 0.2, respectively. (b) Continuous wavelet transform of the signal in figure a. (c) Wavelet transform modulus maxima lines WTMML, obtained from figure b. (d) Amplitude-versus-scale (AVS) curves, measured along the modulus maxima lines in figure c. The slopes ($\alpha = -0.4$, 0, 0.2) correspond to the singularity exponents of the signal in figure a.

We will now show that the exponent α can be obtained straightforwardly from this wavelet transform, following the method introduced by Mallat and Hwang [13] and adopted by Herrmann [8] and Goudswaard and Wapenaar [7]. Replacing z by σz and z' by $\sigma z'$ in Eq. (1) yields

$$\check{c}(\sigma, \sigma z) = \frac{1}{|\sigma|^{\mu}} \int_{-\infty}^{\infty} c(\sigma z') \\ \psi\left(\frac{\sigma z' - \sigma z}{\sigma}\right) \sigma \mathrm{d}z', \tag{4}$$

or, using Eq. (3) for $\sigma > 0$,

$$\check{c}(\sigma, \sigma z) = \sigma^{\alpha+1-\mu} \int_{-\infty}^{\infty} c(z')\, \psi(z' - z)\mathrm{d}z', \tag{5}$$
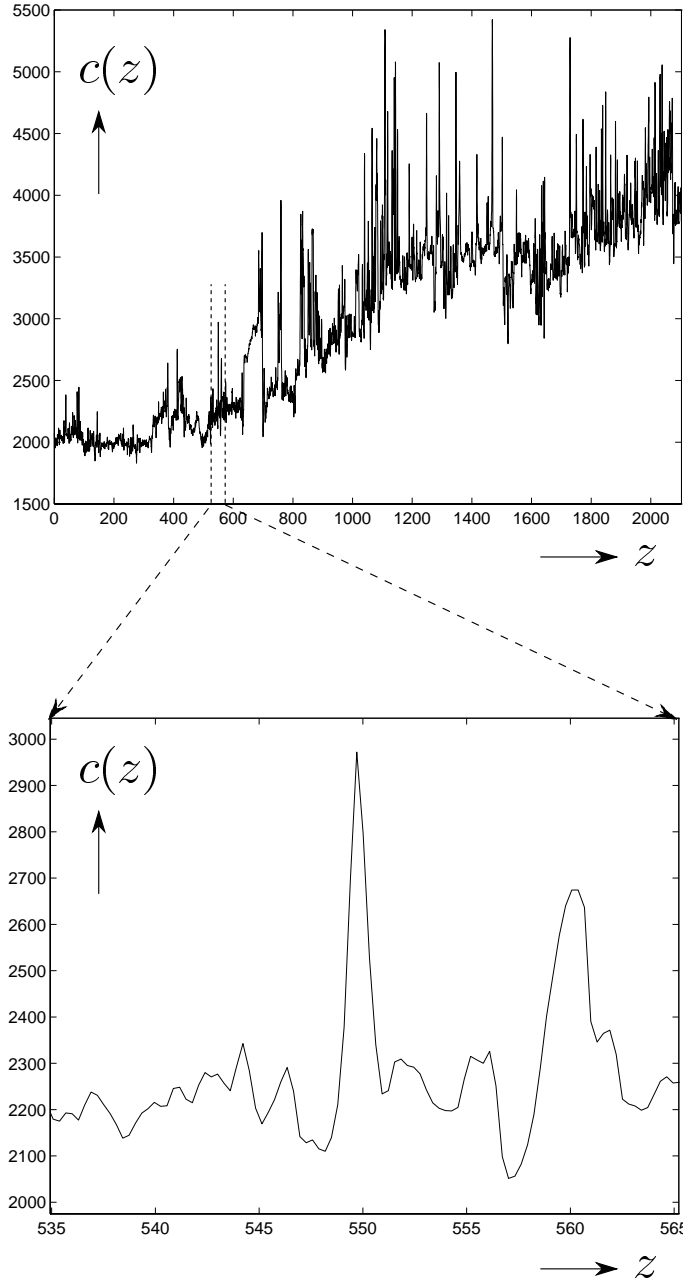
or, comparing the right-hand side with that of Eq. (1) for $\sigma = 1$,

$$\check{c}(\sigma, \sigma z) = \sigma^{\alpha+1-\mu}\, \check{c}(1, z). \tag{6}$$

It appears to be convenient to choose $\mu = 1$, so that Eq. (6) reduces to

$$\check{c}(\sigma, \sigma z) = \sigma^{\alpha}\, \check{c}(1, z). \tag{7}$$

This equation expresses the wavelet transform at an arbitrary scale σ (the left-hand side) in terms of the wavelet transform at a fixed scale $\sigma = 1$ (the right-hand side). We see that for increasing σ the transform dilates ($z \to \sigma z$) and the amplitude changes according to σ^{α}. This behavior is clearly observed in Fig. 1(b) (remember that in the example we chose a negative value for α, hence σ^{α} is a decaying function). The value of the exponent α determines the rate of change of the amplitude. In order to estimate α from $\check{c}(\sigma, \sigma z)$ (Fig. 1(b)) we first take the modulus of both sides of

Fig. 3. Borehole measurements of acoustic propagation velocity $c(z)$.

Eq. (7), according to

$$|\breve{c}(\sigma, \sigma z)| = \sigma^\alpha |\breve{c}(1, z)|, \tag{8}$$

which is represented by the grey-scale in Fig. 1(c). The curved line in this figure connects the local maxima from trace to trace and is called the wavelet transform modulus maxima line (WTMML). Let $z = z_{max}$ denote the z-value for which $|\breve{c}(1, z)|$ reaches a local maxi-

mum. Then

$$|\breve{c}(\sigma, \sigma z_{max})| = \sigma^\alpha |\breve{c}(1, z_{max})| \tag{9}$$

represents the modulus of the wavelet transform along the WTMML. When we take the logarithm (base 2) of the modulus along this line we obtain

$$\log_2 |\breve{c}(\sigma, \sigma z_{max})| = \alpha \log_2 \sigma + \log_2 |\breve{c}(1, z_{max})|. \tag{10}$$
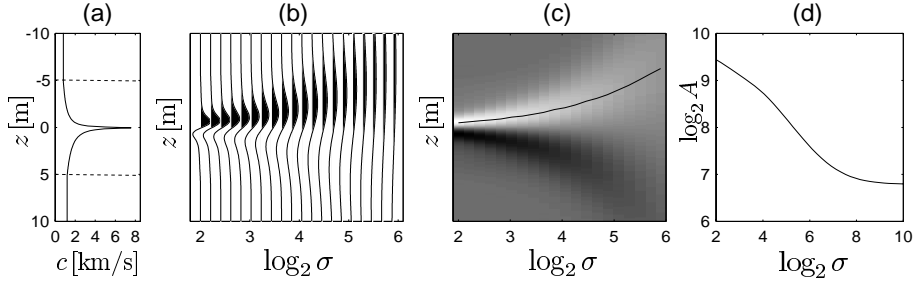
Fig. 4. (a) Self-similar signal, described by Eq. (2), with $\alpha = -0.4$, embedded between two homogeneous half-spaces $z \leqslant -5$ m and $z \geqslant 5$ m. (b) Continuous wavelet transform of the signal in figure a. (c) Wavelet transform modulus maxima line WTMML, obtained from figure b. (d) Amplitude-versus-scale (AVS) curve, measured along the modulus maxima line in figure c. For small σ the slope of the AVS curve in (d) is constant and again given by $\alpha = -0.4$; for large σ the slope approaches zero, as for a step function.
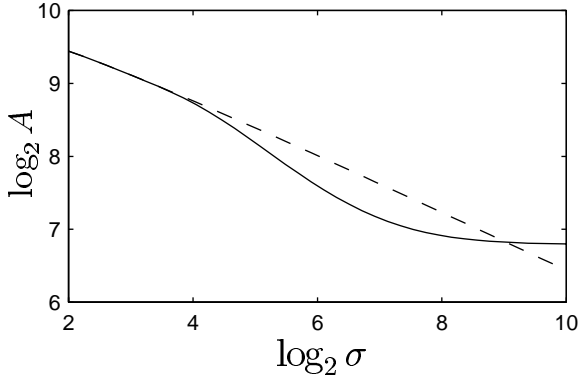

Fig. 5. Comparison of the AVS curves of Figs 4(d) (solid) and 1(d) (dashed). For small scales they are indistinguishable.

The term $\alpha \log_2 \sigma$ shows that, in a log-log representation, the modulus along the WTMML changes linearly with increasing scale, as can also be witnessed from the amplitude-versus-scale (AVS) curve in Fig. 1(d). The rate of change of this amplitude (i.e., the slope of the AVS curve) is equal to α, i.e., the exponent of the signal described by Eq. (2). Note that when we had chosen another value for μ, then the rate of change of the amplitude would be equal to $\alpha + 1 - \mu$.

In Fig. 2(a) we see a signal that consists of three shifted versions of the signal $c(z)$ described by Eq. (2), with values for α of -0.4, 0 and 0.2, respectively (Goudswaard and Wapenaar [7]). Note that for $\alpha = 0$ Eq. (2) represents a step function which jumps from c_1 to c_2. Figure 2(b), (c) and (d) show again the continuous wavelet transform, the WTMMLs and the AVS curves, analogous to those in Fig. 1. The slopes of the AVS curves in Fig. 2(d) are -0.4, 0 and 0.2, respectively, which correspond to the α values of the signal in Fig. 2(a).

Herrmann [8,9] proposed to use the wavelet transform including the WTMML analysis to characterize out-

liers in acoustic borehole data. Figure 2(a) may be seen as a stylistic version of borehole measurements of the acoustic propagation velocity $c(z)$ as a function of the depth in a borehole, see Fig. 3. Of course in reality the function $c(z)$ described by Eq. (2) will represent the acoustic propagation velocity only in an approximate sense and at most in a finite depth interval. To see what happens when we restrict the depth interval, we analyze a velocity outlier described by Eq. (2) for $-z_1 < z < z_1$ (with $z_1 = 5$ m), embedded between homogeneous half-spaces $z \leqslant -z_1$ and $z \geqslant z_1$ with propagation velocities $c_1 = 800$ m/s and $c_2 = 1200$ m/s, respectively, see Fig. 4(a). A similar wavelet analysis as above has been carried out. Note that the slope of the AVS curve in Fig. 4(d) is not constant. For small scales ($\sigma \to 0$) the slope of this AVS curve approaches that in Fig. 1(d). So in this limit the embedding half-spaces have no effect on the scaling behavior. For large scales ($\sigma \to \infty$) the amplitude along the AVS curve is nearly constant (as for a step function), which implies that in this limit the scaling behavior is fully determined by the embedding half-spaces. In Sections 3.3 and 4 we will see that the wavelet transform analysis of real borehole measurements leads to AVS behavior analogous to that in Figs 1(d), 2(d) and 4(d).

We conclude this section by giving a quantitative interpretation of the scales σ in the examples above. The analyzing wavelet that was used is the derivative of a Gaussian, defined as

$$\psi\left(\frac{z}{\sigma}\right) = \frac{\partial}{\partial z}\left[\frac{\exp\left[-\left(\frac{z}{2\sigma\Delta z}\right)^2\right]}{2\sqrt{\pi}}\right], \qquad (11)$$

with $\Delta z = 0.1$ m. The Fourier transform of this wavelet is $j(k\sigma\Delta z)\exp[-(k\sigma\Delta z)^2]$ and reaches its maximum at $k_0 = 1/(\sigma\Delta z\sqrt{2})$. Hence, the effective wavelength of the analyzing wavelet is given by $\lambda_{\text{eff}} = 2\pi/k_0 = 2\sqrt{2}\,\pi\sigma\Delta z$, from which we derive
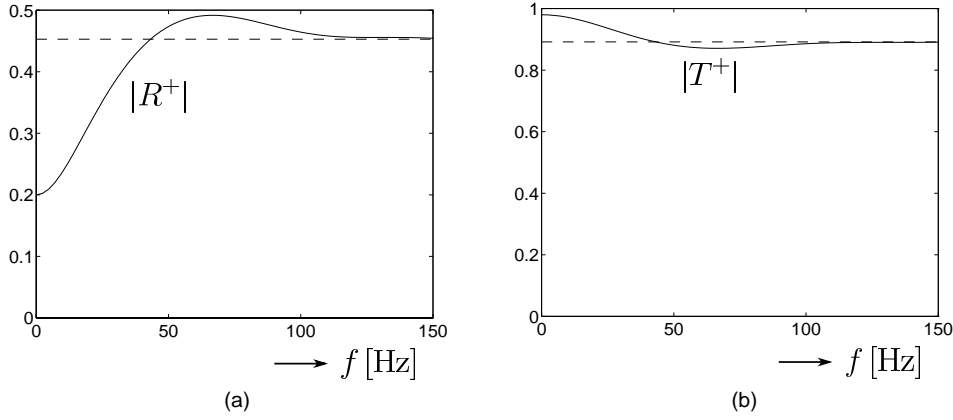
Fig. 6. Modulus of the reflection (a) and transmission (b) coefficients of the embedded self-similar velocity function of Fig. 4(a) (solid) and their high-frequency approximations (dashed).
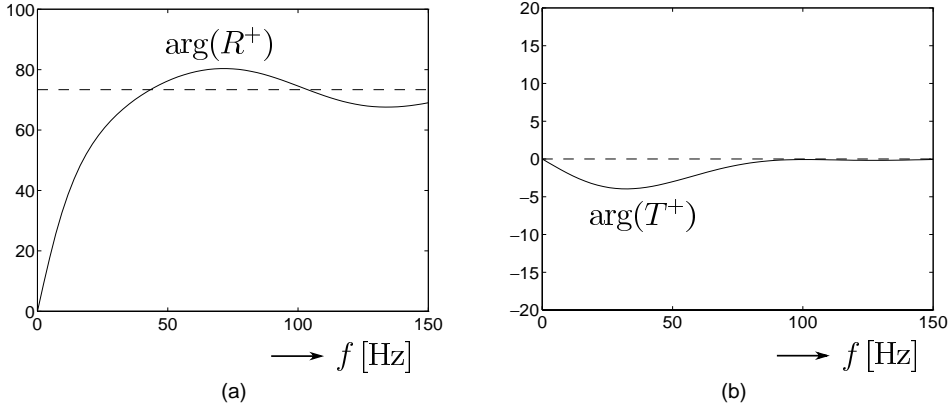

Fig. 7. Phase of the reflection (a) and transmission (b) coefficients of the embedded self-similar velocity function of Fig. 4(a) (solid) and their high-frequency approximations (dashed).

that $\log_2 \sigma = \{2, 4, 6, 8, 10\}$ in Figs 1 and 4 corresponds to $\lambda_{\text{eff}} = \{3.5, 14, 57, 228, 910\}$ m. Of course these wavelengths can not be uniquely related to seismic frequencies, since the velocity is not constant. Using an effective velocity c_{eff} we define the corresponding effective seismic frequency as $f_{\text{eff}} = \frac{c_{\text{eff}}}{\lambda_{\text{eff}}}$. Choosing (quite arbitrarily) $c_{\text{eff}} = 2000$ m/s, we thus find that the above-mentioned range of scales correspond to $f_{\text{eff}} = \{570, 142, 34, 9, 2.2\}$ Hz. Hence, the scales $\log_2 \sigma = 4$ to $\log_2 \sigma = 8$ roughly correspond to the seismic frequency range. In Fig. 5 we observe that the AVS curves of the velocity functions shown in Figs 1 and 4 match very accurately for scales smaller than the seismic scales; within the seismic frequency range they follow a similar trend and for larger scales they are completely different.

3. Linking borehole data with seismic data

Based on the foregoing discussion we choose the self-similar velocity function of Eq. (2) as a parameterization of geological transitions in the Earth's subsurface, as they are observed in borehole measurements. For $\alpha = 0$ it corresponds to a step function from c_1 to c_2, which is the usual parameterization of geological transitions in seismic exploration. The generalization for $\alpha \neq 0$ encompasses a wider class of transitions that amongst others accounts for observed outliers in borehole measurements, see Fig. 3.

In this section we analyze the interaction of seismic waves with geological transitions parameterized as self-similar velocity functions and we derive the relation between the scaling behavior of the velocity function and the seismic reflection data. First we consider the normal incidence case. For this situation we re-

view the properties of the exact reflection and transmission coefficients and discuss their effect on the reflection and transmission responses in relation to the scaling properties of the velocity function. Next we consider the case of oblique incidence. For this situation no explicit expressions are available for the reflection and transmission coefficients. However, it appears to be possible to derive the scaling behavior of the wavelet transform of the reflection response in the ray-parameter scale domain. This scaling behavior is the fingerprint of the seismic response of the geological transition and contains the same parameter α that appears in the wavelet transform of the velocity function. Finally we illustrate the correspondence between the scaling parameters of the borehole- and seismic data with two realistic numerical examples.

3.1. Normal incidence reflection and transmission responses

The exact normal incidence reflection and transmission coefficients for a self-similar velocity function, embedded between two homogeneous half-spaces (Fig. 4(a)), are derived in [22]. In Figs 6 and 7 the modulus and phase of R^+ and T^+ are shown as a function of the frequency.

The low-frequency limits are given by

$$R^+ = -R^- \rightarrow \frac{c_2 - c_1}{c_2 + c_1}, \tag{12}$$

$$T^+ = T^- \rightarrow \frac{2\sqrt{c_2 c_1}}{c_2 + c_1} = \sqrt{1 - (R^+)^2} \tag{13}$$

(the superscripts $+$ and $-$ refer to down- and up going incident waves, respectively). Note that these coefficients are equal to the exact flux-normalized coefficients for a discrete boundary between two homogeneous half-spaces, i.e., for the situation in which the velocity is described by a step function (the density is assumed constant). This is consistent with the multiscale analysis in Fig. 4, which revealed that for large σ the embedded self-similar velocity function behaves as a step function. For the values of c_1 and c_2 chosen in Section 2, Eqs (12) and (13) yield $R^+ = -R^- \rightarrow 0.2$ and $T^{\pm} \rightarrow \sqrt{0.96}$ (see Fig. 6 for $f \rightarrow 0$).

The high-frequency limits (for positive frequency) are given by

$$R^+ = -\{R^-\}^* \rightarrow j \left[\frac{e^{-j\nu\pi} c_2^{2\nu} + e^{j\nu\pi} c_1^{2\nu}}{c_2^{2\nu} + c_1^{2\nu}} \right], \tag{14}$$

$$T^+ = T^- \rightarrow \frac{2 \sin(\nu\pi) \sqrt{c_2^{2\nu} c_1^{2\nu}}}{c_2^{2\nu} + c_1^{2\nu}}, \tag{15}$$

where j is the imaginary unit, $\nu = 1/(2 - 2\alpha)$ with $\alpha < \frac{1}{2}$ and * denotes complex conjugation. Note that these asymptotic expressions are frequency-independent. The factor j in Eq. (14) corresponds to a Hilbert transform in the time domain. For the values of c_1 and c_2 chosen in Section 2 and variable α, the modulus and phase of the high-frequency reflection and transmission coefficients R^+ and T^+ are shown in Fig. 8. For $\alpha = -0.4$ we have $|R^{\pm}| \rightarrow 0.4528$, $\arg(R^+) \rightarrow 73.37°$, $\arg(R^-) \rightarrow 106.63°$, $|T^{\pm}| \rightarrow 0.8916$, $\arg(T^{\pm}) = 0°$. These values (except $\arg(R^-)$) are represented by the dashed lines in Figs 6 and 7. The coefficients in Eqs (14) and (15) are equal to the exact coefficients for the self-similar function of Fig. 1(a) (i.e., without the embedding half-spaces). This is consistent with the multi-scale analysis in Figs 1 and 4, which revealed that for small σ the embedding half-spaces have no effect on the scaling behavior of the velocity function.

Finally we consider the time-domain reflection and transmission responses of the embedded self-similar velocity function shown in Fig. 4(a). For the down going incident wave field we choose a Ricker wavelet, defined by $s_R(t) = (1 - 2\pi^2 f_0^2 t^2) e^{-\pi^2 f_0^2 t^2}$, with $f_0 = 50$ Hz. The Fourier transform of this wavelet is $S_R(f) = \frac{2}{\sqrt{\pi}} \frac{f^2}{f_0^3} e^{-f^2/f_0^2}$. Multiplying this spectrum with the exact complex reflection and transmission coefficients of Figs 6 and 7 and transforming the results back to the time-domain yields the reflection and transmission responses, shown by the solid lines in Fig. 9. In the reflection response a significant phase distortion of the Ricker wavelet is observed, in agreement with Fig. 7(a). The transmission response, on the other hand, has undergone nearly no phase distortion, in agreement with Fig. 7(b). Figure 9 also shows the high-frequency approximations of the reflection and transmission responses, denoted by the crosses $(+)$. These responses have been obtained using the asymptotic reflection and transmission coefficients of Eqs (14) and (15) (see Fig. 8 for $\alpha = -0.4$). Note that the main features of the exact responses are reproduced reasonably well by these high-frequency approximations.

3.2. Scaling properties of the oblique reflection response

We consider again Fig. 2(a) as a stylistic version of borehole measurements of the acoustic propaga-
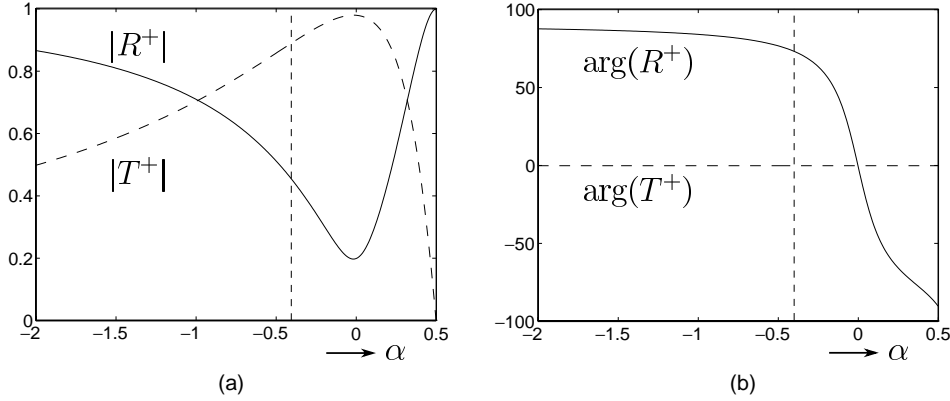
Fig. 8. High-frequency approximation of the modulus (a) and phase (b) of the reflection coefficient R^+ (solid) and the transmission coefficient T^+ (dashed) of the embedded self-similar velocity function of Fig. 4(a). The moduli and phases are plotted as a function of the singularity exponent α. For $\alpha = -0.4$ the moduli and phases correspond to those in Figs 6 and 7 for $f \to \infty$.
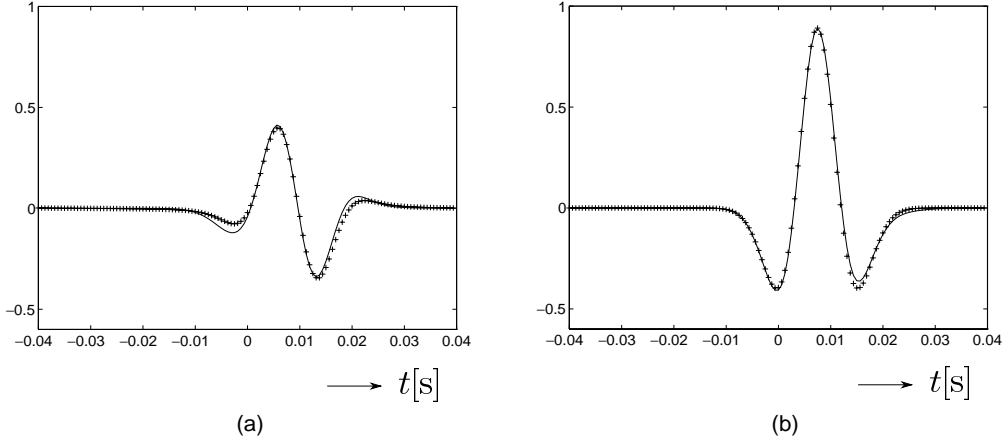

Fig. 9. Reflection (a) and transmission (b) responses of the embedded self-similar velocity function of Fig. 4(a) (solid) and their high-frequency approximations (+).

tion velocity $c(z)$ as a function of the depth in a borehole. Figure 10(a) shows the angle-dependent plane wave response of this velocity function in the ray-parameter intercept-time (p, τ) domain (the ray-parameter p is related to the incident angle ϕ according to $p = \sin \phi / c(0)$). Each trace represents the up going reflection response at the acquisition surface $z = 0$ of a down going plane wave for a particular incident angle ϕ. These reflection responses, which have been modelled by the reflectivity method, have been convolved with a symmetrical seismic wavelet.

The data of Fig. 10(a) can be transformed to the ray-parameter depth (p, z) domain by applying seismic migration per ray-parameter p, using the angle-dependent imaging filters introduced in [23]. The result is an image of the angle-dependent reflectivity in the ray-parameter depth domain, convolved with a p-independent wavelet, as shown in Fig. 10(b). The ray-parameter p is related to the local propagation angle $\phi(z)$ according to $p = \sin \phi(z) / c(z)$, which is constant for all depths (Snell's law).

Next we analyze the wavelet transform of the migrated seismic data. This idea was first proposed by Dessing et al. [2], who used the wavelet transform for multi-scale edge detection in migrated data. Here we discuss an extended procedure that takes the angle-dependent effects into account [23]. We denote the imaged angle-dependent reflectivity of Fig. 10(b) by $r(p, z)$. The wavelet transform $\check{r}(p, \sigma, z)$ is defined, analogous to Eq. (1), as

$$\check{r}(p, \sigma, z) = \frac{1}{|\sigma|^\mu} \int_{-\infty}^{\infty} r(p, z')$$
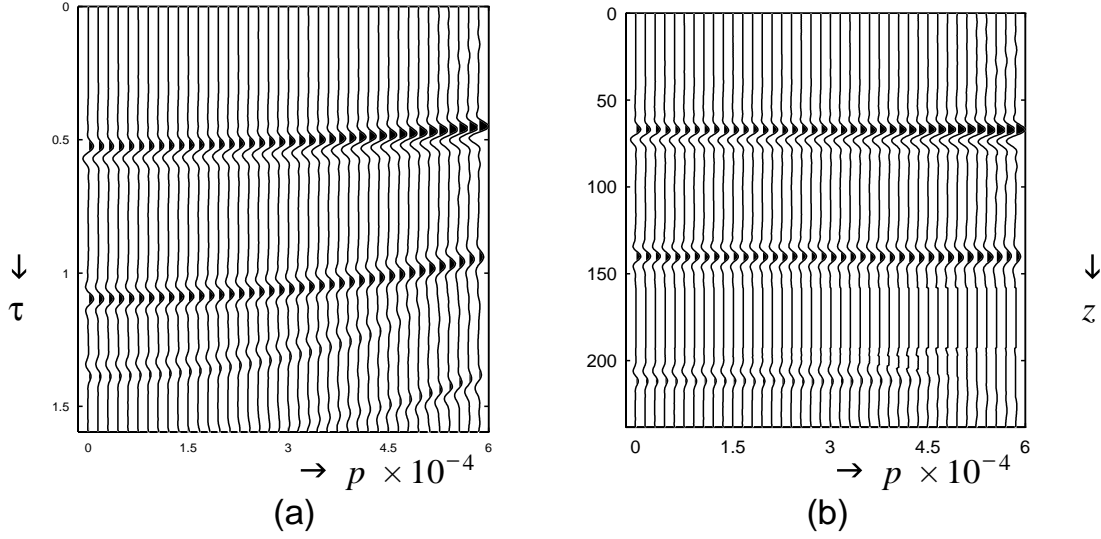
Fig. 10. (a) Plane wave response (p, τ-domain) of the velocity function of Fig. 2(a). (b) Imaged plane wave response (p, z-domain).
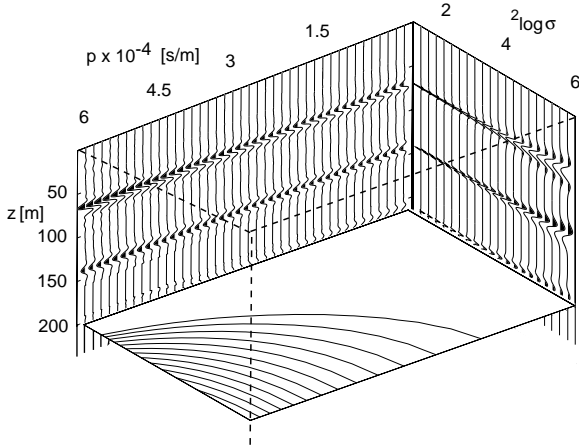

Fig. 11. Multi-scale representation $\breve{r}(p, \sigma, z)$ of the imaged plane wave response of Fig. 10(b).

$$\psi\left(\frac{z'-z}{\sigma}\right)\mathrm{d}z'. \tag{16}$$

Note that according to this equation a one-dimensional wavelet transformation is applied along the z-axis for each p-value. We apply this transform to the data of Fig. 10(b), which are first deconvolved by the p-independent wavelet (Goudswaard and Wapenaar [7]). Figure 11 shows three cross-sections of the wavelet transform $\breve{r}(p, \sigma, z)$ (we used $\mu = 0$ for this example; the reason will be explained later). The left backplane represents the data of Fig. 10(b) in the (p, z) domain. The right backplane shows the wavelet transform of the deconvolved normal incidence trace ($p = 0$). Finally, the horizontal cross-section shows

contours of constant amplitude in a modulus maxima plane (which is the plane that connects the local maxima of $|\breve{r}(p, \sigma, z)|$ for all p and σ, or in other words, it connects the WTMMLs for all p). The amplitude contours in these modulus maxima planes form the fingerprint of the wavelet transformed reflection response and are characteristic for the transitions in the velocity function of Fig. 2(a).

We will now analyze how the contours of constant amplitude in Fig. 11 can be explained quantitatively (see Goudswaard and Wapenaar [7]). Our starting point is the acoustic wave equation in the (p, τ)-domain,

$$\left[\frac{\partial^2}{\partial z^2} - \left(\frac{1}{c^2(z)} - p^2\right)\frac{\partial^2}{\partial \tau^2}\right]u(z, p, \tau) = 0, \tag{17}$$

with $c(z)$ defined by Eq. (2) (hence, in the following analysis, $z = 0$ refers again to the depth of the singularity). Replacing z by βz (with $\beta > 0$), substituting Eq. (3) and multiplying the result by β^2 gives

$$\left[\frac{\partial^2}{\partial z^2} - \left(\frac{1}{c^2(z)} - (\beta^\alpha p)^2\right)\frac{\partial^2}{\partial(\beta^{\alpha-1}\tau)^2}\right]$$
$$u(\beta z, p, \tau) = 0. \tag{18}$$

The term between the square brackets is the same as in Eq. (17), with p replaced by $\beta^\alpha p$ and τ replaced by $\beta^{\alpha-1}\tau$. Hence, Eq. (18) is satisfied by $u(z, \beta^\alpha p, \beta^{\alpha-1}\tau)$ as well as $u(\beta z, p, \tau)$. Consequently,

$$u(z, \beta^\alpha p, \beta^{\alpha-1}\tau) = f(\alpha)u(\beta z, p, \tau), \tag{19}$$
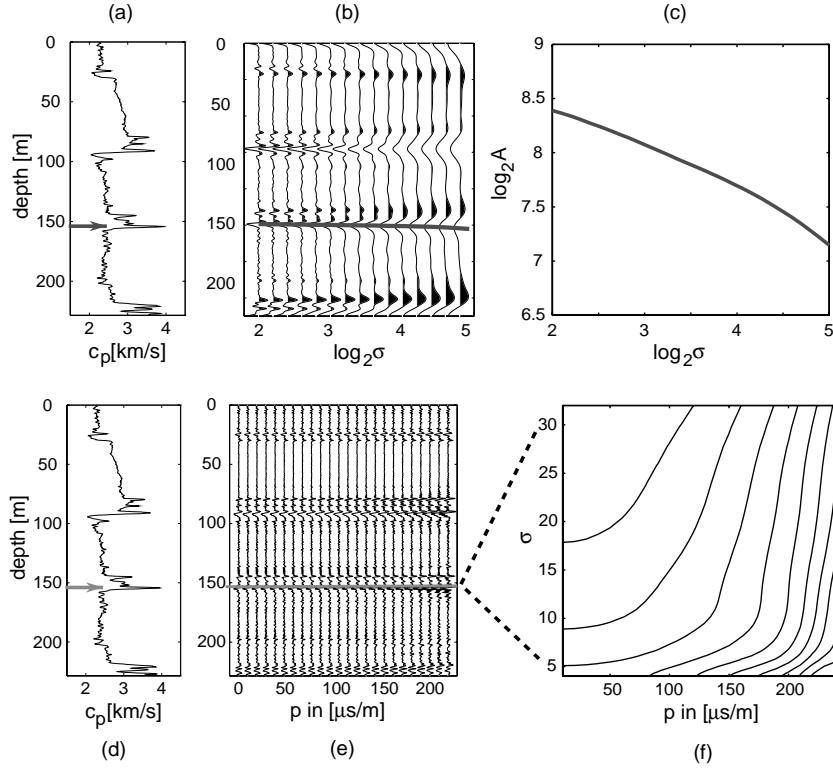
Fig. 12. (a,b,c) Multi-scale analysis of a self-similar velocity transition in a borehole: $\alpha = -0.32$. (d,e,f) Multi-angle multi-scale analysis of its seismic response: $\alpha = -0.34$.

where $f(\alpha)$ is an undetermined α-dependent factor. In the upper half-space $z < 0$ we define an 'incident' wave field u^{inc} and a 'reflected' wave field u^{refl}, both obeying Eq. (19) with one and the same factor $f(\alpha)$. For our analysis we do not need to specify this decomposition any further. We relate these incident and reflected wave fields via a reflection kernel $r(p, \tau)$, according to

$$u^{\text{refl}}(-\epsilon, p, \tau) = \int_{-\infty}^{\infty} r(p, \tau - \tau')$$
$$u^{\text{inc}}(-\epsilon, p, \tau')\mathrm{d}\tau', \tag{20}$$

with $\epsilon \to 0$. Replacing ϵ by $\beta\epsilon$ (with $\beta > 0$), substituting Eq. (19) for u^{inc} and u^{refl} and comparing the result with Eq. (20) shows that the reflection kernel obeys the following similarity relation

$$r(p, \tau) = \beta^{\alpha-1} r(\beta^{\alpha} p, \beta^{\alpha-1}\tau). \tag{21}$$

We introduce the wavelet transform of $r(p, \tau)$ by

$$\check{r}(p, \sigma, \tau) = \frac{1}{|\sigma|^{\mu}} \int_{-\infty}^{\infty} r(p, \tau')$$
$$\psi\left(\frac{\tau' - \tau}{\sigma}\right)\mathrm{d}\tau'. \tag{22}$$

Substituting Eq. (21), replacing τ' by $\beta^{1-\alpha}\tau'$ and $\mathrm{d}\tau'$ by $\beta^{1-\alpha}\mathrm{d}\tau'$ yields

$$\check{r}(p, \sigma, \tau) = \frac{(\beta^{\alpha-1})^{\mu}}{|\beta^{\alpha-1}\sigma|^{\mu}} \int_{-\infty}^{\infty} r(\beta^{\alpha} p, \tau')$$
$$\psi\left(\frac{\tau' - \beta^{\alpha-1}\tau}{\beta^{\alpha-1}\sigma}\right)\mathrm{d}\tau'. \tag{23}$$

Comparing the right-hand side with that of Eq. (22) gives

$$\check{r}(p, \sigma, \tau) = (\beta^{\alpha-1})^{\mu} \check{r}(\beta^{\alpha} p, \beta^{\alpha-1}\sigma, \beta^{\alpha-1}\tau). \tag{24}$$

It now appears to be convenient to choose $\mu = 0$, so that Eq. (24) reduces to

$$\check{r}(p, \sigma, \tau) = \check{r}(\beta^{\alpha} p, \beta^{\alpha-1}\sigma, \beta^{\alpha-1}\tau). \tag{25}$$

Let $\tau = \tau_{\max}$ denote the τ-value for which $|\check{r}(p, \sigma, \tau)|$ reaches a local maximum for fixed p and σ. A modulus maxima plane connects the local maxima $|\check{r}(p, \sigma, \tau_{\max})|$ for all p and σ. It follows from Eq. (25) that the reflection amplitude in a modulus maxima plane behaves as

$$|\check{r}(p, \sigma, \tau_{\max})| = |\check{r}(\beta^{\alpha} p, \beta^{\alpha-1}\sigma, \beta^{\alpha-1}\tau_{\max})|. \tag{26}$$
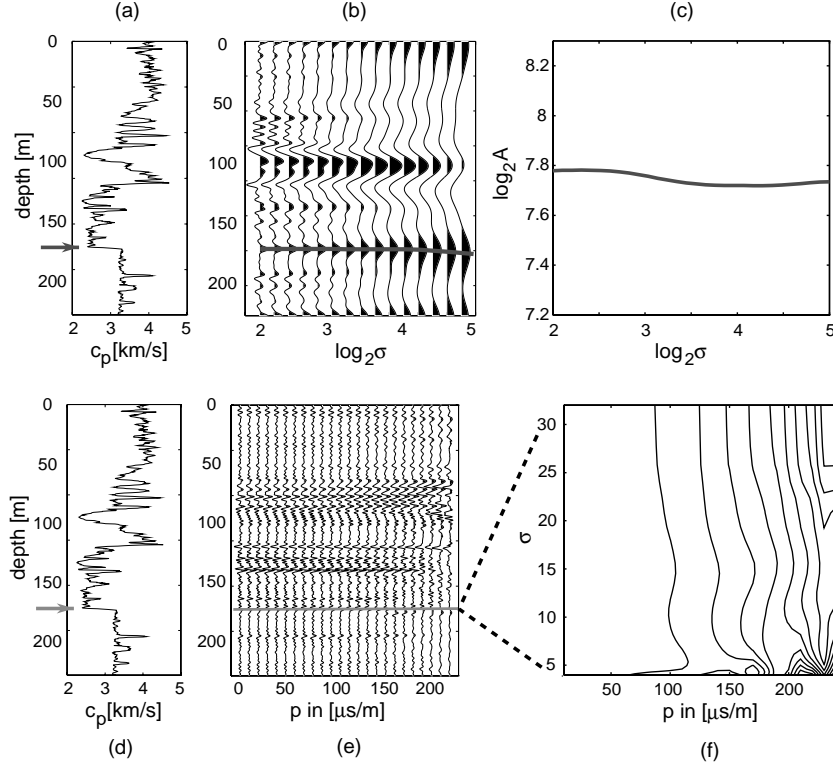
Fig. 13. (a,b,c) Multi-scale analysis of a velocity step-function in a borehole: $\alpha = 0.0$. (d,e,f) Multi-angle multi-scale analysis of its seismic response: $\alpha = 0.03$.

The latter equation implies that contours of constant reflection amplitude in a modulus maxima plane are described by

$$p^{1-\alpha}\sigma^{\alpha} = \text{constant}. \tag{27}$$

Note that the above results have been derived for the wavelet transform of the reflection kernel $r(p, \tau)$ of a self-similar velocity function around $z = 0$. The imaged reflections in Fig. 10(b) represent shifted versions of the reflection kernel as a function of depth instead of intercept time. The results above apply equally well to $\check{r}(p, \sigma, z)$. In particular, the contours of constant amplitude $|\check{r}(p, \sigma, z_{\max})|$ in the modulus maxima plane in Fig. 11 are described by Eq. (27), with $\alpha = 0.2$. This value corresponds to the slope of the third AVS curve in Fig. 2(d). This links the third reflection event in Fig. 10(b) to the third transition in the velocity function of Fig. 2(a).

3.3. Numerical examples

We illustrate the procedure discussed in the previous subsection with two more realistic numerical examples in Figs 12 and 13 (Goudswaard and Wapenaar [7]).

Figure 12(a,b,c) shows a multi-scale analysis of real borehole measurements of the acoustic propagation velocity, analogous to Fig. 1. The slope of the AVS curve in Fig. 12(c) ($\alpha = -0.32$) characterizes the transition at $z = 155$ m in the velocity function of Fig. 12(a). We numerically modelled the seismic response of the velocity function in Fig. 12(a) and applied seismic migration per ray-parameter p. The resulting angle-dependent seismic image is shown in Fig. 12(e). Figure 12(f) shows the multi-angle multi-scale analysis of the deconvolved imaged seismic response, analogous to the horizontal plane in Fig. 11 (here only the p, σ-plane at $z = 155$ m is shown). It appears that the contours in Fig. 12(f) are approximately described by $p^{1-\alpha}\sigma^{\alpha} = \text{constant}$, with $\alpha = -0.34$. Note that this corresponds very well to the value obtained directly from the borehole measurements. Figure 13 shows a similar example, but this time the analyzed velocity transition at $z = 170$ m clearly resembles a step-function ($\alpha = 0$). Note that the contours in Fig. 13(f) show that for this situation the imaged seismic response is nearly scale-*in*dependent, as expected (the contours are approximately described by $p = \text{constant}$, which is Eq. (27) for $\alpha = 0$).
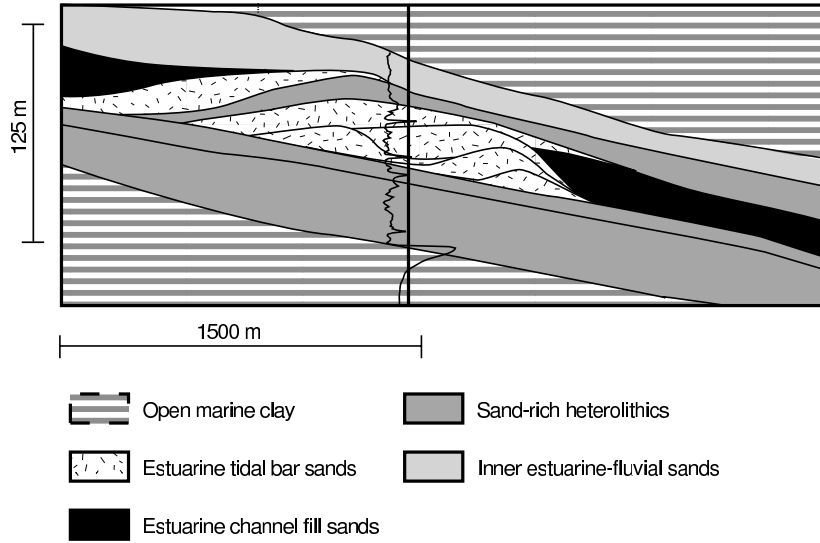
Fig. 14. Geological model of the Cook Formation. The detailed impedance function is displayed in overlay at $x = 1500$ m.
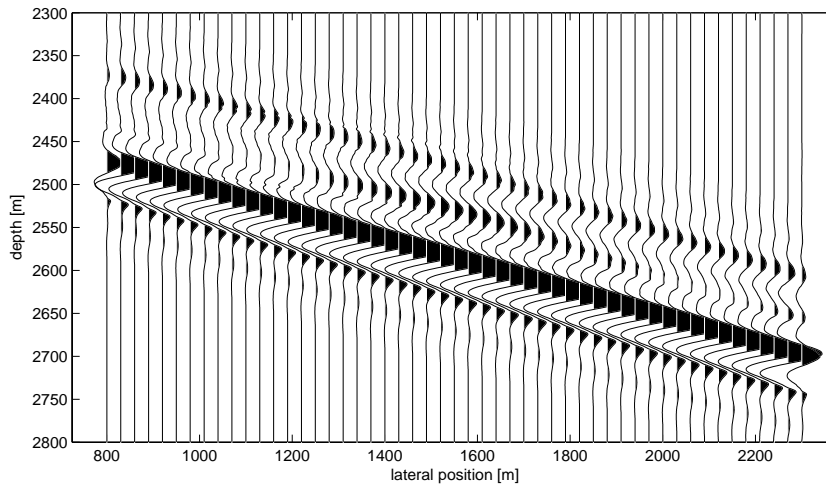

Fig. 15. Simulated migrated seismic section for the geological model of Fig. 14.

We may conclude that the amplitude behavior in the modulus maxima planes of the seismic reflection response is indeed characteristic for the velocity transitions in the borehole measurements. For a velocity step-function [Eq. (2) with $\alpha = 0$] the contours described by Eq. (27) are straight lines defined by $p = \text{constant}$, hence, any deviation from these straight lines indicates that we are dealing with a velocity transition, other than a step-function. The α-values derived from the contours in the modulus maxima planes of the seismic reflection response correspond to the slope of the AVS curves of the velocity transitions in the borehole measurements.

4. Linking geological models with seismic data

To assess complex geological subsurface models it is useful to have an accurate and efficient way of generating seismic data that can be compared with real seismic data. Given a realization of a geological subsurface model, one could generate seismic data by numerical forward modelling and subsequently apply an imaging procedure (seismic migration) in order to simulate a seismic subsurface image. This simulated image could then be compared with an image obtained from real seismic data and based on this comparison the geological model could be either accepted or updated. The
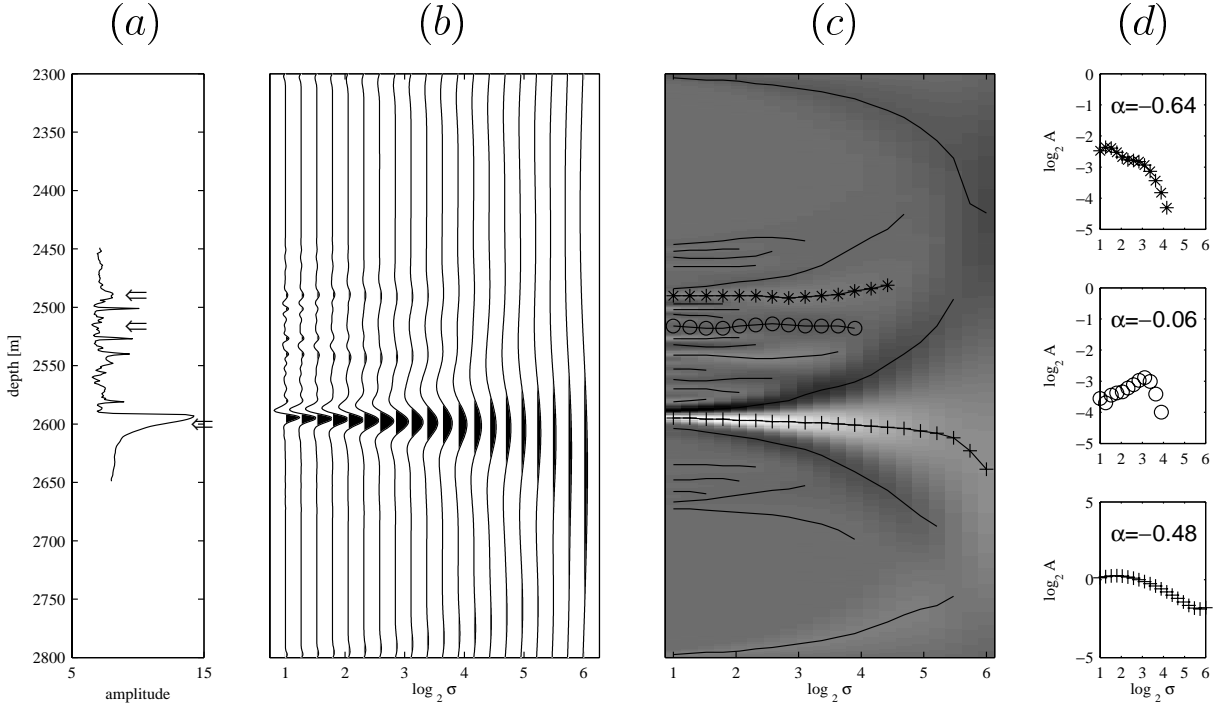
Fig. 16. Wavelet transform analysis of the geological model of Fig. 14. (a) Vertical cross-section of the impedance function of the geological model at $x = 1500$m. (b) Continuous wavelet transform of the impedance function in figure a. (c) Wavelet transform modulus maxima lines (WTMMLs), obtained from figure b. (d) Amplitude-versus-scale (AVS) curves, measured along the modulus maxima lines in figure c.

advantage of this procedure is that the simulated and real seismic data are compared in the depth domain. Since this is also the domain of the geological model, this facilitates the geological interpretation. However, a disadvantage is that seismic modelling and seismic migration are computationally expensive techniques. Since finding a suited geological model would require iterative application of modelling and migration, this proposal is unattractive from a practical point of view.

Fortunately it appears to be possible to combine the processes of seismic modelling and seismic migration into one operator which can be applied very efficiently in comparison with the two individual processes. This combined operator maps the geological model in the depth domain directly to simulated migrated data in the depth domain. The main effect of this operator is that it limits the spatial resolution of the geological model both in the vertical as well as in the lateral direction. For this reason we also refer to this operator as the spatial resolution function. The process of obtaining the simulated seismic migrated data thus comes to convolving the 2-D or 3-D geological subsurface model with this resolution function. For the 3-D situation this is described by

$$m(x, y, z) = s(x, y, z) * r(x, y, z), \qquad (28)$$

where $r(x, y, z)$ is the reflectivity of the geological subsurface model, $s(x, y, z)$ denotes the spatial resolution function (the convolution kernel) and $m(x, y, z)$ denotes the simulated migrated seismic data. The asterisk refers to the spatial convolution along the x-, y- and z-axes. The spatial resolution function depends on the macro velocity properties of the geological model as well as on the acquisition configuration. In general it will vary from place to place, hence, Eq. (28) actually describes a space-variant spatial convolution process. The idea of using resolution functions to efficiently simulate migrated seismic data was introduced by Schuster and Hu [18]. Toxopeus et al. [19] proposed to use this procedure to efficiently assess complex geological models. For a typical 2-D model the computation time for one iteration (i.e., assessing one realization of a geological model) is in the order of seconds if one uses the resolution function, whereas applying full seismic modelling and migration would require a computation time in the order of hours for each iteration. It should be noted that the current practice of assessing complex geological models is based on a 1-D convolution method to generate simulated seismic data (see Pratson and Gouveia [15] for a recent example). This 1-D method only accounts for the vertical resolution
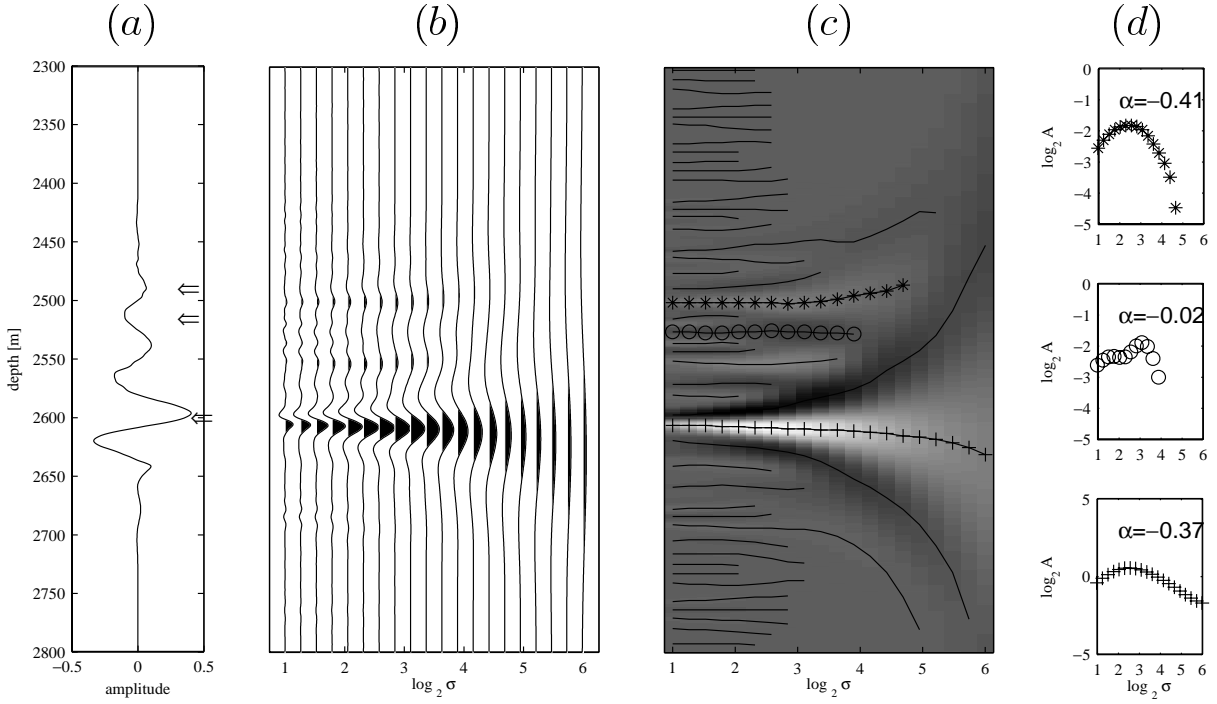
Fig. 17. Wavelet transform analysis of the simulated migrated section of Fig. 15. (a) Vertical cross-section of the migration result at $x = 1500$ m. (b) Continuous wavelet transform of figure a. (c) Wavelet transform modulus maxima lines (WTMMLs), obtained from figure b. (d) Amplitude-versus-scale (AVS) curves, measured along the modulus maxima lines in figure c.
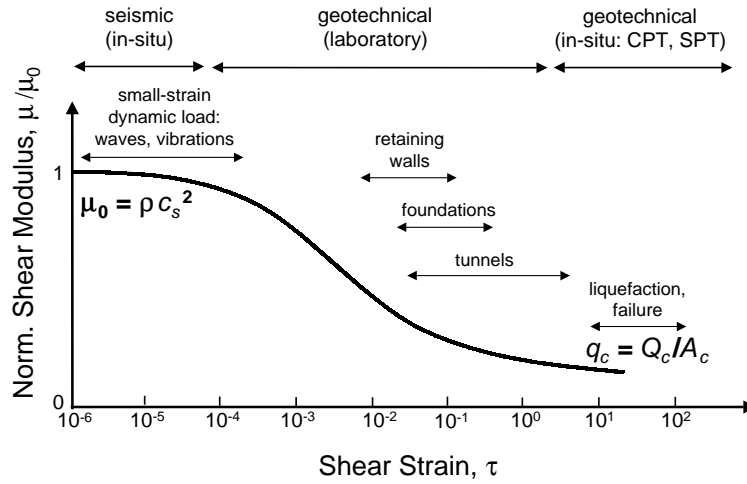

Fig. 18. Schematic illustration showing various soil testing approaches corresponding to various strain levels and various problem areas. Note that seismic and CPT represent, respectively, two extreme ends of this very large range of strains; hence, they indicate very different soil properties. In this figure, μ_0 is the shear modulus or stiffness at very small strain, and q_c is the CPT cone resistance.

in seismic data. On the other hand, the method outlined above accounts for the lateral as well as the vertical resolution and thus yields more realistic simulated migrated data.

The wavelet transform, and in particular the analysis of WTMMLs as discussed in Section 2, provides a tool to link facies in the geological model to reflection events in simulated as well as in real migrated data. Let the geological model be described by the detailed impedance function $I(x, y, z)$. Analogous to Eq. (1),
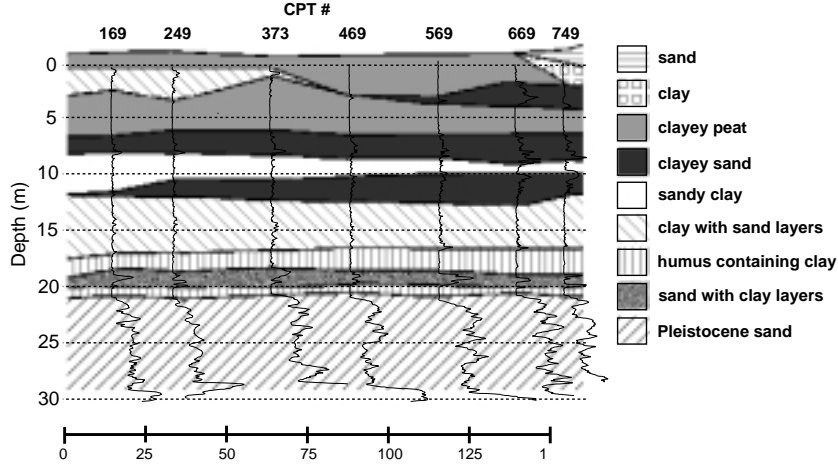
Fig. 19. Soil profile derived from the CPT data and from the continuous soil sampling in a number of boreholes. CPT q_c data (displayed in overlay) defined the layer boundaries, while the soil sampling results determined the composition/type of the soil. Note the distinct lateral variations in the fine-scale CPT data along the boundary between two layers. The location of this profile corresponds with that of the seismic line.

the wavelet transform of $I(x, y, z)$ is defined as

$$\check{I}(\sigma, x, y, z) = \frac{1}{|\sigma|^{\mu_1}} \int_{-\infty}^{\infty} I(x, y, z') \psi_1\left(\frac{z' - z}{\sigma}\right) \mathrm{d}z', \tag{29}$$

where x and y are parameters. The choice for the analyzing wavelet $\psi_1(z)$ and the exponent μ_1 will be discussed later. Similarly, the wavelet transform of the (simulated) migrated data $m(x, y, z)$ is defined as

$$\check{m}(\sigma, x, y, z) = \frac{1}{|\sigma|^{\mu_2}} \int_{-\infty}^{\infty} m(x, y, z') \psi_2\left(\frac{z' - z}{\sigma}\right) \mathrm{d}z', \tag{30}$$

where $\psi_2(z)$ and μ_2 may be different from $\psi_1(z)$ and μ_1. We derive a relation between $\check{m}$ and $\check{I}$. First, using Eq. (28) we may write

$$\check{m}(\sigma, x, y, z) = s(x, y, z) * \check{r}(\sigma, x, y, z), \tag{31}$$

where

$$\check{r}(\sigma, x, y, z) = \frac{1}{|\sigma|^{\mu_2}} \int_{-\infty}^{\infty} r(x, y, z') \psi_2\left(\frac{z' - z}{\sigma}\right) \mathrm{d}z'. \tag{32}$$

Next we approximate the reflectivity function $r(x, y, z)$ by

$$r(x, y, z) \approx \frac{1}{2\bar{I}} \frac{\partial I(x, y, z)}{\partial z}, \tag{33}$$

where $\bar{I}$ is an averaged (possibly smoothly varying) version of the impedance function $I(x, y, z)$. Substitution into Eq. (32) and applying integration by parts yields for positive σ

$$\check{r}(\sigma, x, y, z) \approx -\frac{1}{2\bar{I}} \frac{1}{\sigma^{\mu_2+1}} \int_{-\infty}^{\infty} I(x, y, z') \psi_2'\left(\frac{z' - z}{\sigma}\right) \mathrm{d}z', \tag{34}$$

where $\psi_2'(z) = \frac{\partial \psi_2(z)}{\partial z}$. When we choose

$$-\psi_2'(z) = \psi_1(z), \tag{35}$$

$$\mu_2 + 1 = \mu_1 \tag{36}$$

and compare the result for positive σ with Eq. (29), we find

$$\check{r}(\sigma, x, y, z) \approx \frac{\check{I}(\sigma, x, y, z)}{2\bar{I}}, \tag{37}$$

or, using Eq. (31),

$$\check{m}(\sigma, x, y, z) \approx s(x, y, z) * \frac{\check{I}(\sigma, x, y, z)}{2\bar{I}}. \tag{38}$$

Hence, if we make the choices for the wavelets and exponents according to Eqs (35) and (36), it follows from Eq. (38) that the wavelet transform of the (simulated) migrated data is approximately proportional to the wavelet transform of the geological model (in terms of the impedance) convolved with the spatial resolution function. When the resolution function is derived for a seismic wavelet that has a constant spectrum in the seismic frequency band, it thus follows that the AVS behavior along the WTMMLs of the migrated data is ap-
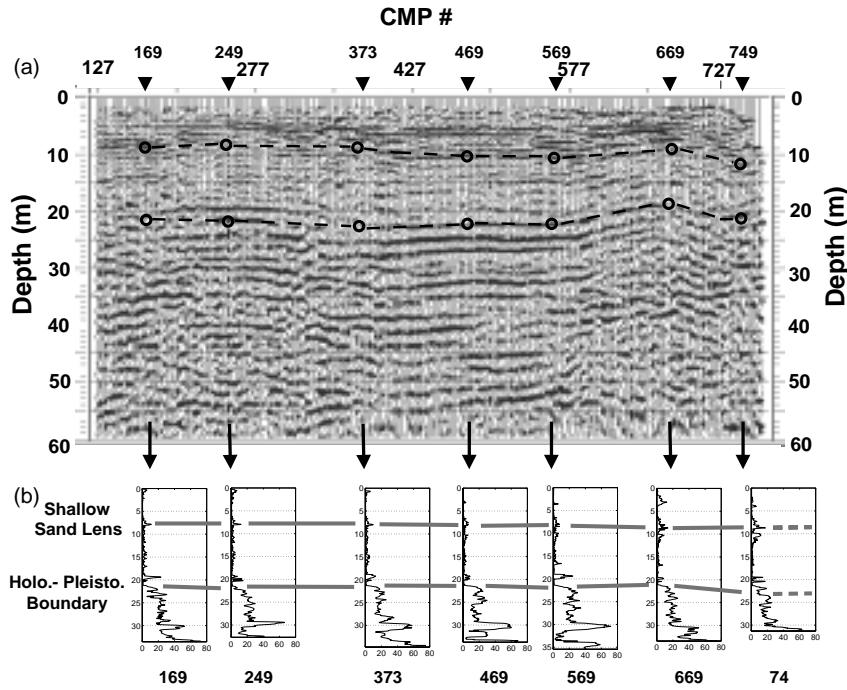
Fig. 20. (a) Shallow shear wave depth section. (b) CPT data at 7 locations (black triangles) along the seismic line. Two strong events (marked by gray lines) identified on both the CPT and seismic data are the ones for which the wavelet transform analysis has been performed in order to check the relation between the CPT and seismic data.
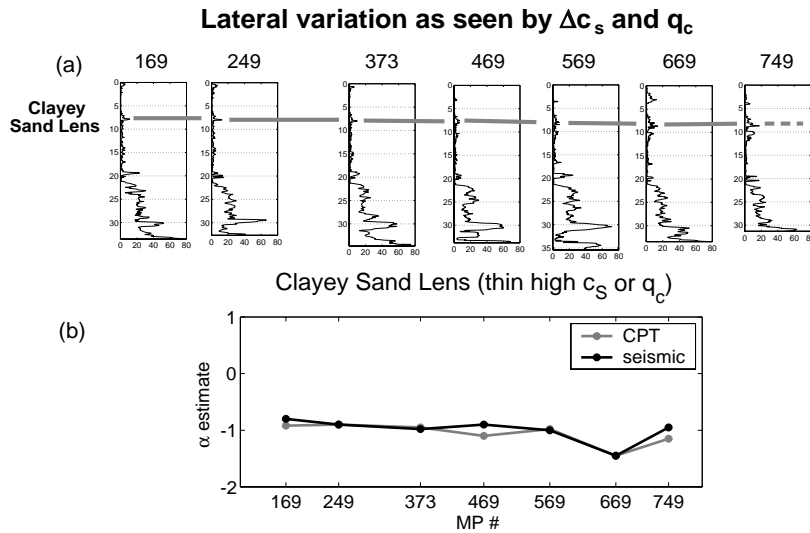

Fig. 21. Comparison of α values of the CPT and the shallow shear wave seismic data for the clayey sand lens at 7.5–9.0 m depth. (a) The chosen shallow event in the CPT data. (b) Estimated α for CPT (grey) and seismic (black).

proximately equal to that of the geological model. This facilitates linking specific reflections in the (simulated) migrated data to facies in the geological model.

We discuss this procedure at the hand of a small numerical 2-D case study. The Cook Formation in the Os-

eberg field, offshore Norway, is the focus in this study. The depositional setting, genetic types and large scale geometry of the Cook Formation were derived by analysis of the available cores, wire-line logs and seismic lines. The Cook Formation is an estuarine infill with
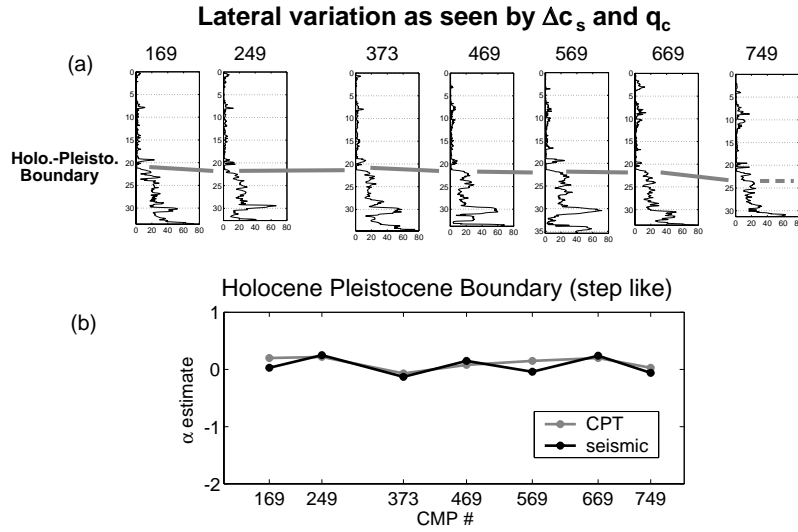
Lateral variation as seen by Δc$_s$ and q$_c$

Fig. 22. Comparison of α values of the CPT and the shallow shear wave seismic data for the Holocene-Pleistocene boundary at 21–22 m depth. (a) The chosen deep event in the CPT data. (b) Estimated α for CPT (gray) and seismic (black).

a strong tidal and fluvial influence, the envelope of the entire sequence is an elongated funnel. Using the envelopes of regionally correlated sequences as a framework, a more detailed quantitative facies model of the sedimentary architecture was built with sedimentological data of the Gironde tidal estuary (SE France) as an analogue. Relevant impedance values derived from wire-line data were assigned to the facies models. The geological model of the Cook Formation, obtained with a geological model builder (Petersen [14]) is shown in Fig. 14. The grayscales in this figure represent different facies types; the more detailed impedance function (derived from velocity and density logs) is shown in overlay at $x = 1500$ m. This model was used as input to create an idealized 2-D simulated migrated seismic section, using the procedure of Toxopeus et al. [19], see Fig. 15. The wavelet transform of a vertical cross-section of the geological model (i.e., the impedance function at $x = 1500$ m) was obtained according to Eq. (29), using for $\psi_1(z)$ a Ricker wavelet (i.e., minus the second derivative of a Gaussian) and choosing $\mu_1 = 1$. The result is shown in Fig. 16. Note that the AVS curves in Fig. 16(d) show a behavior that is more complex than the constant slope behavior we observed in previous examples (the α-values depicted in this figure denote average slopes; they do not capture the complex behavior of these AVS curves). Figure 17 shows the wavelet transform of the simulated migrated data at $x = 1500$ m, using Eq. (30) with $\psi_2(z)$ being the first derivative of the Gaussian and $\mu_2 = 0$. Note that the AVS curves in Fig. 17(d) show trends that correspond

quite well with those in Fig. 16(d). This confirms that we can identify events in the simulated migrated data with transitions in the impedance function of the geological model. This is one step of the iterative scheme outlined above. The next aim is to find similar links between simulated migrated data derived from a geological model and migrated field data and use this to improve the geological model. This is the subject of ongoing research of Toxopeus.

5. Linking geotechnical data with shallow seismic data

A cone penetration test (CPT) is the most common geotechnical testing method used to estimate in-situ the strength properties of the soil of the shallow subsurface. In CPT, a cone at the end of a series of rods is pushed into the ground at a constant rate and measurements are made of the resistance to the penetration of the cone. This is known as 'cone resistance' or q_c, which is the total force (Q_c) acting on the cone divided by the projected area (A_c) of the cone. The cone resistance q_c is a direct indicator of the strength of the soil at a given depth. Although CPT provides valuable information on the strength of the soil, the information is restricted to the CPT location.

In recent years there have been attempts to check whether the shallow high-resolution seismic reflection method, particularly that using shear waves, could be used to define the lateral continuity or variability of the

soil layers of different strengths as seen by CPT (see e.g. Ghose et al. [5]). Seismic methods measure the small strain response of a relatively large volume of ground whereas the penetration of the cone locally measures the large strain response of the ground since the average stress levels around the cone approximately equal failure of the soil. Thus, seismic and CPT represent soil properties that correspond to very different levels of strain. Figure 18 schematically illustrates the order of strains corresponding to various measurements and the nonlinear strain-dependency of soil deformation. The seismic shear velocity c_s relates to the very small strain (order $10^{-5} - 10^{-6}$) elastic properties of the soil, specifically the small-strain shear modulus or rigidity, while CPT cone resistance q_c represents the failure or strength properties at very large strains (typically > 10). Thus there is a strain difference in the order of a million. Despite the fact that c_s and q_c are physically very different quantities, recent experiments consistently show the existence of relations between them (see Ghose and Goudswaard [4] for an extensive list of references). Empirical relationships have been proposed based on these observations (see the references in [4]). Recently also correlations have been observed in field data between shear wave reflections and sharp transitions in CPT cone resistance q_c [5]. Ghose and Goudswaard [4] propose to use the wavelet transform analysis to CPT and shallow seismic data to link events in both data types. We illustrate their procedure with a real data example.

An extensive field experiment was carried out at a site where multiple CPTs were located directly on the seismic line. Hence, any subtle variation at an interface could directly be compared between seismic and CPT data. The surface condition was flat and grass-covered. The shallow geology at this site is composed of alternating layers of sand and clay. At the shallowest part there are peat layers which act as important cap soil from environmental consideration. The Holocene-Pleistocene boundary is situated at around 21–22 m depth. Figure 19 shows a detailed soil profile at this site exactly below the seismic line. This profile was derived by interpolation of data from many CPTs (see the CPT q_c plots in this figure), supplemented by data of testing of soil samples in a few boreholes. The seismic data were acquired using for the source a small horizontal vibrator, developed for controlled generation of high-frequency shear waves (30–500 Hz), see Ghose et al. [3]. Data processing was carried out, carefully preserving the amplitude information. The processing included suppression of surface waves and multiples,

followed by inversion of the angle-dependent reflection information into shear wave velocity contrasts (Δc_s; not shown). Figure 20(a) shows the seismic depth section and Fig. 20(b) shows q_c data from 7 CPTs located along the seismic line; the CPT locations are shown by black triangles on the top of the seismic section. It is clear that the shear wave reflections follow the strong q_c transitions quite well. However, the characteristic properties of the q_c transitions, which vary laterally as can be clearly seen in the CPT data, cannot be discriminated in the seismic section. The multi-scale analysis using the wavelet transform has been used to analyze the laterally varying properties of transitions in the CPT and in the seismic data. We chose 2 prominent transitions in the CPT data (Fig. 20(b)). One is at a depth around 7.5–9.0 m, corresponding to a sand-clay boundary, and another is at around 22 m depth, corresponding to the Holocene-Pleistocene boundary. For these two strong laterally continuous events, we carried out the wavelet transform analysis for both the CPT (q_c) and the seismic data (Δc_s). Figure 21(a) shows the chosen shallow event in the CPT data. Figure 21(b) shows the α values derived from the AVS curves along the WT-MMLs of the CPT q_c data as well as from the seismic Δc_s data. From 21(b) we observe that the estimates of the singularity parameter α for CPT and seismic are remarkably close. This result illustrates that it is possible to link the laterally varying information of the CPT q_c data to the Δc_s information in the shear-wave reflection data. Figure 22(b) illustrates the result of applying the wavelet transform analysis to CPT and seismic data for the chosen deeper event, i.e., the prominent Holocene-Pleistocene boundary (Fig. 22(a)). Again we observe a remarkable similarity of the α-estimates from CPT and seismic data. These results are striking because they clearly demonstrate that shear wave reflection data contain information of the local scaling behavior of the soil strength as seen by CPT measurements.

6. Conclusions

We have shown that the continuous wavelet transform, and in particular the analysis of amplitudes along wavelet transform modulus maxima lines (WTMMLs) as proposed by Mallat and Hwang [13], is a powerful tool to analyze the characteristic properties of local variations in a signal. The amplitude-versus-scale (AVS) curve of a particular transition in a signal can be seen as its fingerprint. When different types of measurements are used to probe the same subsurface region,

each of the data types can be analyzed with the wavelet transform. If one understands the physics underlying the different types of measurements one may 'tune' the different wavelet transforms in such a way that a particular geological transition leaves the same fingerprint in the wavelet transform of each data type. In this way the wavelet transform can be used as a tool that aids the integration of different types of data.

Acknowledgements

References

[1] F.J. Dessing, *A wavelet transform approach to seismic processing*, PhD thesis, Delft University of Technology, 1997.

[2] F.J. Dessing, E.V. Hoekstra, F.J. Herrmann and C.P.A. Wapenaar, *Multiscale edge detection by means of multiscale migration*, in: Soc. Expl. Geophys., Expanded Abstracts, 1996, pp. 459–462.

[3] R. Ghose, J. Brouwer and V. Nijhof, *A portable S-wave vibrator for high-resolution imaging of the shallow subsurface*, in Eur. Assoc. Expl Geophys., Extended Abstracts, 1996, Session: M037.

[4] R. Ghose and J.C.M. Goudswaard, Integrating S-wave seismic-reflection data and cone-penetration-test data using a multiangle multiscale approach, *Geophysics* **69** (2004), 440–459.

[5] R. Ghose, V. Nijhof and J. Brouwer, *Shallow, high-resolution, shear-wave reflection imaging: extended potential in geotechnical surveys*, In Proc. of the Environ. Eng. Geophys. Soc. Europ. Sec. Mtg., 1998, pp. 419–422.

[6] J.C.M. Goudswaard, *Multiangle multiscale characterization of seismic reflection data*, PhD thesis, Delft University of Technology, 2001.

[7] J.C.M. Goudswaard and C.P.A. Wapenaar, Scale and angle dependent reflection properties of self-similar interfaces, *Journal of Computational Acoustics* **9** (2001), 1015–1023.

[8] F.J. Herrmann, *A scaling medium representation*, PhD thesis, Delft University of Technology, 1997.

[9] F.J. Herrmann, *Evidence of scaling for acoustic waves in multiscale media and its possible implications*, In Soc. Expl. Geophys., Expanded Abstracts, 1998, pp. 1684–1687.

[10] G. Kaiser, *A friendly guide to wavelets*, Birkhäuser, Boston, 1994.

[11] P. Kumar and E. Foufoula-Georgiou, Wavelet analysis in geophysics: an introduction, in: *Wavelets in Geophysics*, P. Kumar and E. Foufoula-Georgiou, eds, Academic Press, Inc, 1994, pp. 1–43.

[12] S. Mallat, *A wavelet tour of signal processing*, Academic Press, San Diego, 1998.

[13] S.G. Mallat and W.L. Hwang, Singularity detection and processing with wavelets, *IEEE Trans. Inform. Theory* **38**(2) (1992), 617–643.

[14] S.A. Petersen, *Compound modelling – a geological approach to the construction of shared earth models*, In Eur. Assoc. Expl Geophys., Extended Abstracts, 1999, Session 5–12.

[15] L.F. Pratson and W. Gouveia, Seismic simulations of experimental strata, *AAPG Bulletin* **86** (2002), 129–144.

[16] E.A. Robinson, *Predictive decomposition of seismic traces with applications to seismic exploration*, PhD thesis, Massachusetts Institute of Technology, 1954.

[17] E.A. Robinson, *Seismic inversion and deconvolution: Dual-sensor technology. – Handbook of Geophysical Exploration*. Pergamon, Amsterdam, 1999.

[18] G.T. Schuster and J. Hu, Green's function for migration: Continuous recording geometry, *Geophysics* **65** (2000), 167–175.

[19] G. Toxopeus, S.A. Petersen and C.P.A. Wapenaar, *Improved geological modeling and interpretation by simulated migrated seismics*, in: Soc. Expl. Geophys., Expanded Abstracts, 2003, pp. 1829–1832.

[20] A.J. van Wijngaarden, *Imaging and characterization of angle-dependent seismic reflection data*, PhD thesis, Delft University of Technology, 1998.

[21] F. Verhelst, *Integration of seismic data with well-log data*, PhD thesis, Delft University of Technology, 2000.

[22] C.P.A. Wapenaar, Seismic reflection and transmission coefficients of a self-similar interface. *Geoph. J. Int.* **135** (1998), 585–594.

[23] C.P.A. Wapenaar, W.J.F. van Geloven, J.C.M. Goudswaard, A.J. van Wijngaarden and F.J. Dessing, AVA migration and multiscale characterization in finely layered media, *J. Seismic Expl.* **6** (1997).